Scaling of the Detonation Product State
with Reactant Kinetic Energy

Scott I. Jackson

Shock and Detonation Physics (M-9)
Los Alamos National Laboratory
Los Alamos, NM 87545 USA

Abstract

Chemical explosives provide one of the most high-power and energy-dense storage materials available. During detonation, transfer of this energy to adjacent materials is governed by the detonation product equation of state. No accurate methodology exists for prediction of this thermodynamic relationship and equation-of-state data continues to be experimentally characterized for each new formulation or charge density. Here we present a universal detonation product equation of state derived from several newly discovered empirical correlations in prior condensed-phase detonation product measurements. This model depends only on initial charge density and detonation velocity as inputs, dramatically simplifying the calibration process relative to existing models, which require measurement of up to seven formulation-specific parameters. This new result implies the product energy density scales with reactant kinetic energy density, which is the product of the explosive initial density and detonation velocity squared, for all condensed-phase energetic materials and that explosive microstructural or chemical details only influence the product energy density though these two parameters.

Keywords: detonation, product equation of state, heat of detonation, detonation velocity, high explosive

1. Introduction

Detonating condensed-phase explosives produce product energy densities approaching 14 MJ/L and energy release rates exceeding 1 TW/m^2, which is higher than the radiative flux at the solar surface. Despite extensive use in the mining and defense industries for several centuries, no accurate methodology exists for prediction of the detonation product equation of state (EOS), which governs the transfer of energy from the products to adjacent materials. This work is typically achieved though pressure-volume expansion of the detonation products, as their high pressure exceeds the yield strength of all known materials. The product EOS and detonation velocity D_0, constitute the two most important parameters to designers of explosive systems. Efforts to theoretically or empirically unify all explosive product measurements have had only limited success [1–6].

Models have also been developed to estimate D_0 and product EOS parameters from thermochemical equilibrium assumptions [7, 8]. While these models are continually being improved, they rely heavily on assumed reaction zone kinetics and detonation product species that are not directly measured or known for most high explosive detonation flows. Instead, they are empirically calibrated to existing D_0, EOS data, and assumed final product states, which can be insufficient to fully constrain their predictions. Thus, equation-of-state data continues to be experimentally characterized for each new formulation, charge density and scale, which requires an expensive and specialized series of tests and analysis [9].

Measurement of the product EOS and D_0 can prove challenging as they vary locally in a charge depending on formulation, density, scale, and shape variation. Additionally, the product states behind the detonation wave are extreme, approaching 40 GPa and 4000 K with significant optical opacity. These conditions render conventional thermodynamic-sensing flow diagnostics useless and advanced light source test facilities cannot yet accommodate large enough charges to recreate the detonation reaction zone conditions present in engineering-scale explosive systems. Thus, traditional explosive product EOS measurement techniques continue to involve detonation of large metal-confined charges and infer the product EOS from the resulting high-rate metal deformation. Prior to this work, each explosive EOS measurement has been considered distinct with no capability to relate EOS's from different explosive formulations or densities to one another.

Here, the discovery of a universal EOS for detonation products is reported that is based on the identification of multiple empirical correlations in product EOS data that have not been previously observed. This common product model utilizes

2

only two material-specific measurable parameters, the explosive initial density ρ_0 and D_0, to predict the detonation product isentrope. This approach is a dramatic simplification of current EOS models that rely on seven or more parameters, many of which cannot be directly measured. The existence of this common product model, which approximates the product state of all known condensed-phase explosives, implies that, to leading order, the explosive product EOS is independent of microstructure and chemical details.

2. Background

In a steady detonation, shock passage though an explosive adiabatically compresses the metastable reactants and induces onset of exothermic chemical reaction. The energy release then is thought to drive the reacting flow to a locally sonic state, which isolates the reaction zone from downstream perturbations. Of the total chemical energy released e_0, a portion referred to here as the Rayleigh energy e_{RL} is used to support the shock wave's mechanical compression of the reactants and the remainder is the heat of detonation Δh_d, which is stored in the products as internal or kinetic energy. For one-dimensional flow, the thermodynamic path of the detonation is shown in Fig. 1. Shock compression drives the explosive to the von Neumann state defined by the intersection of the Rayleigh line and the reactant Hugoniot. Chemical reaction then expands the flow down the Rayleigh line to the sonic state, where the product Hugoniot is tangent to the Rayleigh line. (The Chapman-Jouguet and sonic states are identical for one-dimensional flow.) The flow subsequently expands down the product isentrope in the absence of any additional shocks. Material is defined as reactant when it is upstream of the shock, reaction zone flow when it is between the shock and sonic surface, and products when it is downstream of the sonic surface. Additional flow dimensionality does not alter these physics qualitatively, but does allow for a flow component normal to the shock, which can result in transversely varying thermodynamic properties.

In practice, the product parameters are inferred from an experimental cylinder expansion test that consists of a ductile metal tube filled with explosive [10]. After explosive detonation, the tube wall is accelerated by the products. Knowledge of the explosive initial density ρ_0 and measurement of the detonation velocity D_0 yield the Rayleigh line, while analysis of the tube motion with a computational or analytical hydrodynamic model is used to infer the product isentrope along with the thermodynamic state of the sonic point [9, 11, 12]. (During this analysis, the detonation is generally approximated as one-dimensional, thus yielding a single
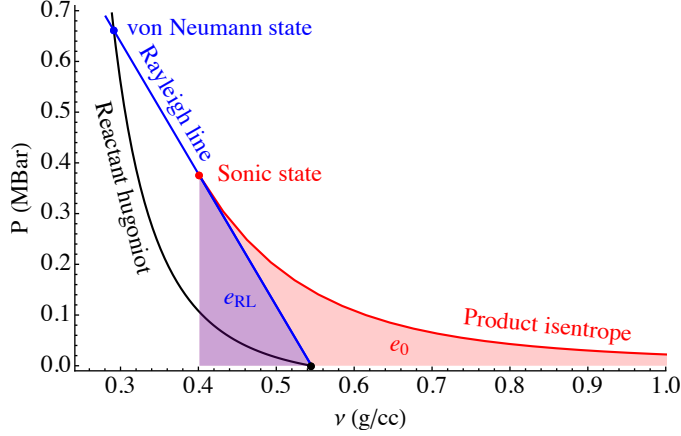
Figure 1: Thermodynamic paths relevant to detonation in P–ν space for PBX 9501 explosive. Reactant Hugoniot, Rayleigh line, and product isentrope are black, blue, and red curves, respectively. The initial, von Neumann, and sonic states are represented by the black, blue, and red points, respectively. The red shading represents e_0, overlapping blue shading representing e_{RL}, and $\Delta h_d = e_0 - e_{RL}$.

sonic state.) Isentropes are then fit to an analytic EOS form, typically the JWL (Jones-Wilkins-Lee) EOS, for concise presentation [11].

The JWL is an incomplete EOS developed for use with condensed-phase explosive products [11]. Consisting of the sum of three functions that are dominant at different product volumes and yielding perfect gas behavior ($P\nu^{1+\omega} = $ constant) at lower pressures, the JWL pressure equation on the principle isentrope is

$$P\left(\Lambda\right) = Ae^{-R_1\Lambda\Delta_s} + Be^{-R_2\Lambda\Delta_s} + C\left(\Lambda\Delta_s\right)^{-(1+\omega)}$$

where $\Delta_s = \nu_s/\nu_0$ and $\Lambda = \nu/\nu_s$ with ν as the specific volume, $_s$ denoting the sonic state condition, and $\nu_0 = 1/\rho_0$. We have introduced Λ via the algebraic expansion $\Delta = \Lambda\Delta_s$ where $\Delta = \nu/\nu_0$ to later plot JWL data at volumes relative to those of the sonic state.

Pressure is related to the energy on the isentrope I by

$$\left(\frac{\partial e}{\partial \Lambda}\right)_I = \Delta_s \left(\frac{\partial e}{\partial \Delta}\right)_I = -\Delta_s P \tag{1}$$

with e as the energy density or energy per unit volume, which is dimensionally equivalent to pressure. The product energy along the principle isentrope is thus

$$e\left(\Lambda\right) = \frac{A}{R_1}e^{-R_1\Lambda\Delta_s} + \frac{B}{R_2}e^{-R_2\Lambda\Delta_s} + \frac{C}{\omega}\left(\Lambda\Delta_s\right)^{-\omega} \quad .$$

4

These equations can also be utilized with the Gruneisen parameter to generate thermodynamic conditions away from the principle isentrope [11, 13].

The JWL equations have eight calibration parameters, five of which are dimensional (A, B, C, ν_s, and ν_0) and three of which are nondimensional (R_1, R_2, and ω). Cylinder expansion data is usually valid to $\Delta < 10$ and $P \approx 0.001$ MBar, which is sufficient to constrain the A, B, R_1, R_2, and ν_s terms. Parameter ν_0 is measured before testing. Thermochemical equilibrium calculations or detonation calorimetry measurements are generally used to constrain the C and ω terms [11, 14]. Calibration parameters of the JWL for many different explosives, as derived primarily from cylinder expansion tests, are available in published literature with many reproduced in Table A.3. In general, they are able to predict cylinder wall expansion velocities to within $\pm 0.5\%$ [11]. The Davis EOS is also less commonly used to fit detonation product EOS data and involves a similar number of calibration parameters [15].

3. Product Parameter Scaling

Figure 2 plots Δh_d and e_{RL} as determined in previous work for many explosive formulations versus $S = \rho_0 D_0^2$, the kinetic energy of the reactants in the shock frame. The filled circles represent Δh_d measured by detonation calorimetry in 12.7-mm-diameter charges [14, 16]. Ornellas [16] only measured Δh_d and we have paired this data with D_0 values corrected for charge size, density, and confinement as determined from separate sources using similar scale tests. The calorimetry data and sources are listed in Table A.2. The crosses denote Δh_d values and the triangles are their corresponding e_{RL} values, as derived from JWLs primarily calibrated to cylinder tests, including those listed in Table A.3. The e_{RL} data is seen to follow a strong linear trend in S. The Δh_d trend is approximately $\sqrt{S}$ at low values and S^1 at the largest measured values. The experimental calorimetry data exhibits relatively little scatter in comparison to the Δh_d JWL data, whose Δh_d value is highly dependent on thermochemical equilibrium assumptions for the product species. In this sense, calorimetry measurements provide a more direct estimate of Δh_d.

Such relationships have not been previously recognized and imply that both Δh_d and e_{RL} scale with S across all explosive formulations, to leading order. Secondary effects are also apparent with two explosives classes deviating from the trend. Insensitive explosives, composed of TATB and LLM-105 base molecules, are low relative to the global data trend for both Δh_d and e_{RL}. Aluminized explosives exhibit substantial scatter, but trend to higher Δh_d.

5
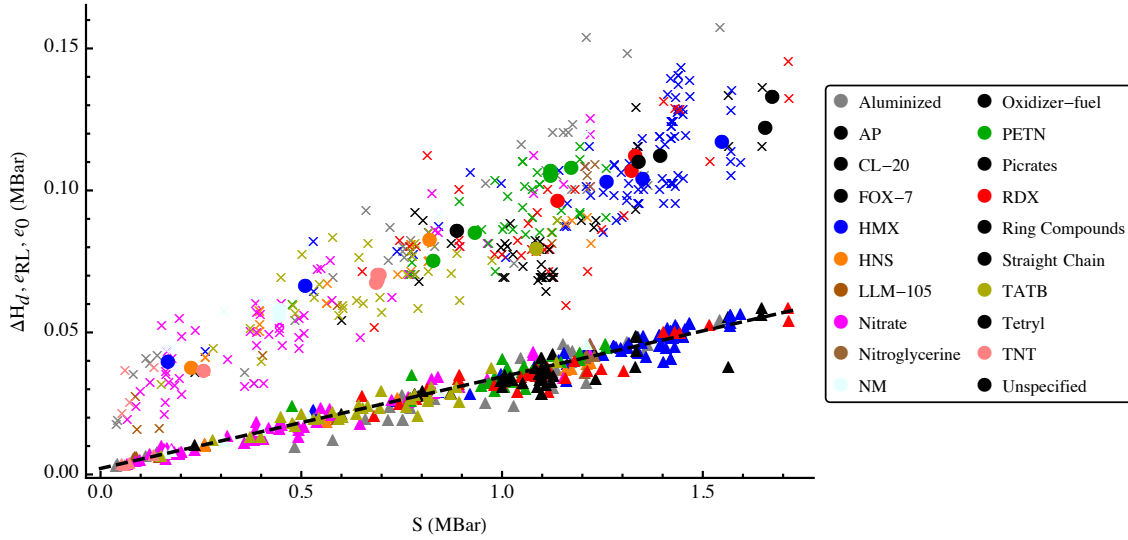
Figure 2: Enthalpies of detonation (circles from calorimetry and crosses from JWLs) and of mechanical compression (triangles) versus S. Symbol color indicates the major explosive component.

The trend observed for Δh_d also occurs at finite product expansions. Figure 3 shows $e(\Lambda)$ versus S for $\Lambda = 1$, 1.4, 3, and 100 as computed all JWLs. The energies represent the remaining internal energy in the products and decrease with increasing Λ, approaching zero as $\Lambda \to 0$. Figure 4 plots $\Delta_s P$ versus S for similar values of Λ as computed from the JWLs. As with $e(\Lambda)$, $\Delta_s P(\Lambda) \to 0$ as $\Lambda \to 0$. Less scatter is apparent relative to $e(\Lambda)$ as P is derived exclusively from experimental cylinder wall motion with no thermochemical assumptions. The curves fit to the data are from the model discussed below.

The adiabatic index γ, governs the partitioning of internal and kinetic energy during compressible motion [13, 17]. In general, γ is the negative logarithmic slope of the isentrope. At the sonic state,

$$\gamma_s \equiv -\frac{\partial \ln P}{\partial \ln \nu}\Big|_s = \frac{1 - P_0/P_s}{\nu_0/\nu_s - 1}$$

and yields

$$\frac{\nu_s}{\nu_0} = \frac{\gamma_s}{\gamma_s + 1} \tag{2}$$

and

$$\frac{P_s}{\rho_0 D_0^2} = \frac{1}{\gamma_s + 1} \, . \tag{3}$$

6

Figure 3: JWL product energies versus S at $\Lambda = 1$ (blue), 1.4 (yellow), 3 (green), and 100 (red). Open triangles and diamonds denote insensitive and aluminized explosives, respectively. The top plot is linear, while the bottom is log-linear scale.

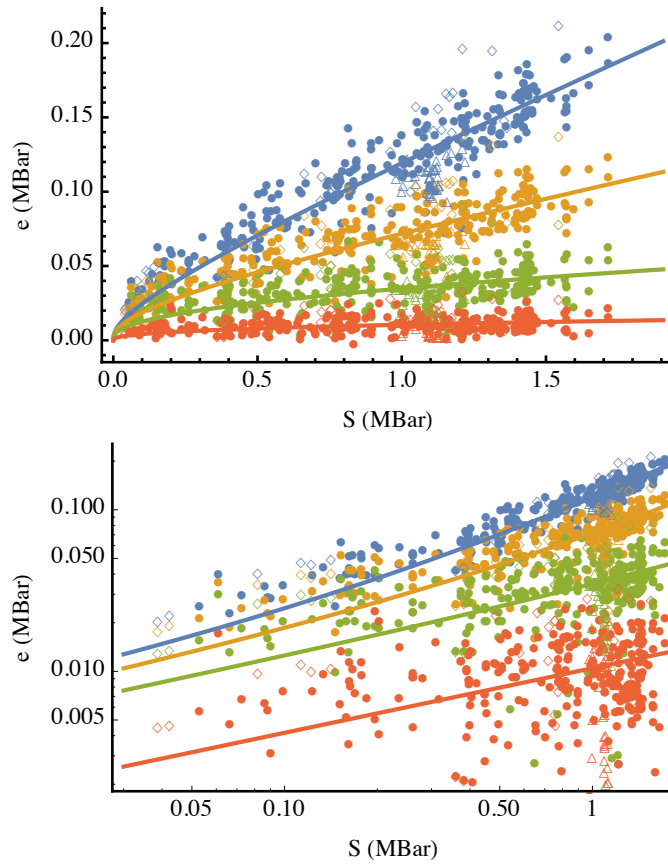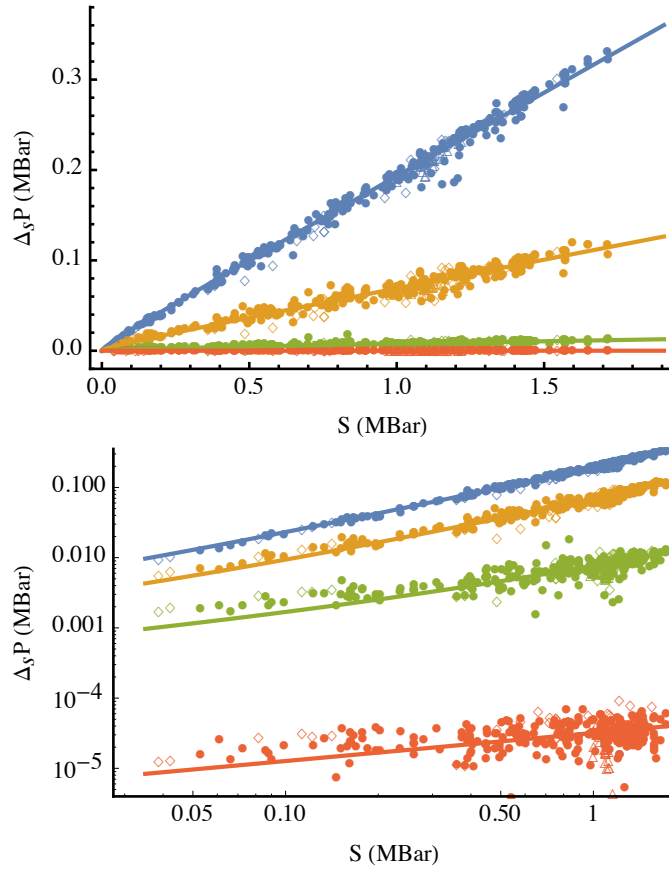Figure 4: The product of JWL pressures and the sonic surface relative volume versus S at $\Lambda = 1$ (blue), 1.4 (yellow), 3 (green), and 100 (red). Open triangles and diamonds denote insensitive and aluminized explosives, respectively. The top plot is linear, while the bottom is log-linear scale.
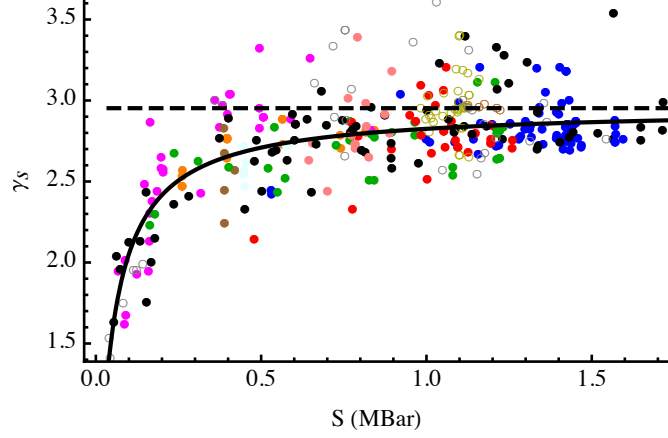
Figure 5: The JWL values of γ_s versus S with the same color scale as Fig. 2. Insensitive and aluminized explosives are plotted with open symbols. Solid curve is from fitted model and dashed line is the model limit as $S \to \infty$.

Values of γ_s, as computed from the JWLs, increase with S (Fig. 5) to asymptotically approach $\gamma_s \approx 2.9$, consistent with the finding that $\gamma_s = 3$ accurately models condensed-phase explosive phenomena in computational studies. As with the previous correlations, the insensitive and aluminized explosives deviate from the trend, in this case towards higher γ_s values.

4. Fitted Model Form and Parameterization

Two key empirical relationships were identified: (1) a linear scaling was observed between e_{RL} and S and (2) a more complex scaling of Δh_d, $e(\Lambda)$, and $\Delta_s P(\Lambda)$ and with S. These can be used to develop a fitted model that is able to predict product isentropes with only ρ_0 and D_0 as inputs.

Calibration methodology for sonic condition

First we address the $\gamma_s(S)$ relationship of Fig. 5. Pairing the empirical observation from Fig. 2 that

$$e_{RL} = M'S + B' \tag{4}$$

with the theoretical definition that $e_{RL} = \frac{1}{2} P_s (1 - \nu_s/\nu_0)$ and utilizing Eqs. 2 and 3 to eliminate P_s and ν_s yields

$$\gamma_s = \sqrt{\frac{S}{2\,(M'S + B')} - 1}\,. \tag{5}$$

9

Simultaneous least squares optimization of M' and B' to the e_{RL} and γ_s data with Eq. 4 and 5 gives the values shown in Table 1. Three solutions are listed. The first "global" set is from a fit to all JWL data except the aluminized and insensitive formulations. The second "insensitive" set is from only fitting the TATB-based and LLM-105-based formulations. The third "aluminized" set is derived from only fitting to formulations containing aluminum.

Table 1: Fit parameters.

	Global	Insensitive	Aluminized
M' (MBar)	3.201×10^{-2}	2.493×10^{-2}	2.853×10^{-2}
B' (MBar)	2.166×10^{-3}	7.524×10^{-3}	2.369×10^{-3}
m_1 (MBar)	1.252	1.320	1.303
m_2	3.351	3.442	3.439
m_3 (MBar)	9.032×10^{-2}	9.230×10^{-2}	7.468×10^{-2}
m_4	1.012	1.210	1.040
b_1 (MBar)	4.249×10^{-2}	3.218×10^{-2}	6.408×10^{-2}
b_2	3.043×10^{-1}	3.153×10^{-1}	3.005×10^{-1}

Comparison of the fitted model prediction to that of the JWLs can be quantified by calculating the error

$$\delta x\left(\Lambda\right) = \frac{x_{\mathrm{FM}}\left(\Lambda\right) - x_{\mathrm{JWL}}\left(\Lambda\right)}{x_{\mathrm{JWL}}\left(\Lambda\right)} 100\% \tag{6}$$

for a generic variable $x(\Lambda)$ across all JWL calibrations. These fit parameters are sufficient to allow prediction of γ_s with Eq. 4, e_{RL} with Eq. 5, ν_s with Eq. 2, and P_s with Eq. 3. The standard deviations of the errors evaluated with Eq. 6 for γ_s, e_{RL}, ν_s, and P_s are 11.9, 10.2, 3.2, and 8.8%, respectively, using global fit parameters for M' and B'. Equations 4 and 5 with global fit parameters are also plotted against the JWL data in Figs. 2 and 5 for e_{RL} and γ_s, respectively.

Calibration methodology of $P(\Lambda)$ and $e(\Lambda)$

The form of the equation describing the relationship between S versus $e(\Lambda)$ and $P(\Lambda)$ is not immediately apparent. Prior experiments have not recognized this correlation and there is no established theoretical basis for it. We can, however, seek inspiration from a combination of CJ theory and the empirical observation of the linear correlation between e_{RL} and S. Substituting Eq. 5 into Eq. 3 yields

$$P_s = \sqrt{2M'S^2 + 2B'S} \tag{7}$$

which generates an appropriate curve in S–P space. Despite only being valid at the sonic surface, an approximated version of this form is fit to the $e(\Lambda)$ data at values of Λ away from unity with several modifications. First, the terms under the square root are separated to render them more easily integrable. Secondly, it is observed that the $S^{0.5}$ term better fits the data when the power is lowered to 0.4. Finally the M' and B' parameters are redefined and postulated to be only functions of Λ, to generate the following functional form

$$P(\Lambda) = -m'(\Lambda)S - b'(\Lambda)S^{0.4} \tag{8}$$

This equation is integrable, able to match the observed data trend in S–$P(\Lambda)$ space, and smoothly goes to zero as $S \to 0$. Integration of $\Delta_s P(\Lambda)$ with no constant of integration yields

$$e(\Lambda) = m(\Lambda)S + b(\Lambda)S^{0.4} \tag{9}$$

Figures 6 and 7 show the values of b, b', m, and m' obtained from least squares fits of Eqs. 8 and 9 to values of $e(\Lambda)$ and $P(\Lambda)$ computed from the JWL parameters. A smooth trend is observed for b and b', as well as for m and m' at lower Λ. Above $\Lambda > 3$ and 5, the m and m' terms, respectively, become insignificant relative to the b and b' terms resulting in scattered least-squares optimizations for m and m'. Additionally, numerical integration shows that $m(\Lambda) = \int m'(\Lambda)d\Lambda$ and $P(\Lambda) = \int P'(\Lambda)d\Lambda$ with no constants of integration, indicating that Eq. 8 is of a suitable form.
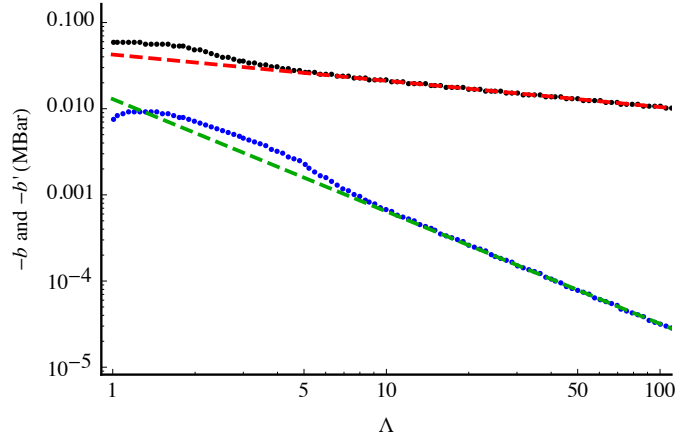
Figure 6: Evolution of $b(\Lambda)$ (black/red) and $b'(\Lambda)$ (blue/green). The black and blue points are the b and b' least-squares fits, respectively, to the global dataset. The red and blue curves are the analytic approximations to b and b', respectively.

11
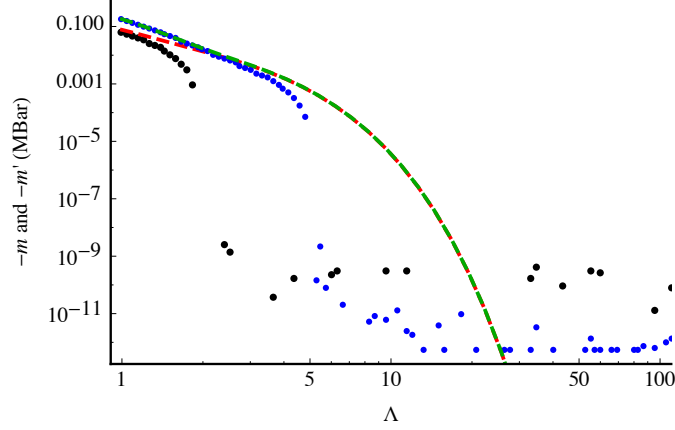
Figure 7: Evolution of $m(\Lambda)$ (black/red) and $m'(\Lambda)$ (blue/green). The black and blue points are the m and m' least-squares fits, respectively, to the global dataset. The red and blue curves are the analytic approximations to m and m', respectively. The scatter in the points below 10^{-7} indicates that the m- and m'-terms can be neglected relative to the b- and b'-terms in those regions.

The computed trends for $m(\Lambda)$ and $b(\Lambda)$ on $e(\Lambda)$ are approximated analytically by

$$m(\Lambda) = m_1 e^{-m_2 \Lambda} + m_3 e^{-m_4 \Lambda}, \tag{10}$$

and

$$b(\Lambda) = b_1 \Lambda^{-b_2} \tag{11}$$

with parameters m_1, m_2, m_3, m_4, b_1, and b_2 listed in Table 1 for the three subsets of explosives. Corresponding values for $P(\Lambda)$ can be found by differentiating Eqs. 10 and 11. This model with the global fit parameters is plotted against the full dataset in Figs. 3 and 4 with good agreement over all Λ.

Figure 8 compares Eq. 7 to Eq. 8 using global-fit parameters. Good agreement is seen between the two forms. The agreement of Eq. 7 to the $S-\Delta_s P$ data is particularly noteworthy since its parameters estimates in Table 1 were only calibrated to the $e_{RL}(S)$ and $\gamma_s(S)$ data, not to the $\Delta_s P(S)$ data.

Fully expanding the fitted model for pressure

$$P(\Lambda) = \Delta_s^{-1} \left(m_1 m_2 S e^{-m_2 \Lambda} + m_3 m_4 S e^{-m_4 \Lambda} + b_1 b_2 S^{0.4} \Lambda^{-(b_2+1)} \right) \tag{12}$$

shows that the equation is very similar the JWL EOS form with three total terms, two of which are exponentials and one of which is a power law. As with the JWL form, the exponential terms in Eq. 12 become negligible in comparison to the power law term at large expansions. Also, the power law exponent terms between

12
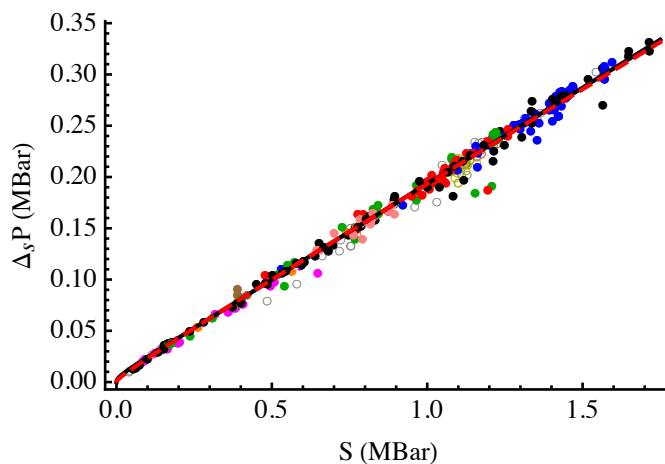
Figure 8: Comparison of Eq. 7 (black curve) and Eq. 8 (red curve) to the experimental data at $\Lambda = 1$ with the same symbol colors as Fig. 2.

the JWL form and Eq. 12 are quantitatively similar. Thus, this new form inherits many of the qualities of the JWL data used to calibrate it, including the anomalous local maxima in γ_s with increasing specific volume [11].

Unlike the JWL, however, the m and b parameters are fixed across broad classes of explosives in Eq. 12 with material specific parameters S and $\nu_s(S, \nu_0)$ used to modulate the amplitude of each term. Thus, Eq. 12 can be viewed as an evolution of the JWL EOS with a reduction of the formulation-specific parameters. The constant m and b parameter values across many formulations indicates empirical identification of new thermodynamic commonalities across all known JWL EOS's. A suggested alternate calibration methodology would be to calibrate this new form directly to a large set of cylinder wall motion data. Such an approach would be a significant effort, but would remove any influence of the JWL model on the final result.

Finally, the author notes that Urtiew and Hayes [3] previously identified a scaling relationship based on the assumption of constant e_0/S and γ_s, implying constant Δ_s and P_s/S. The limited availability of published JWL data at the time of their effort may have prevented them from recognizing the more complex dependence of γ_s and e_0 with S shown in the present study.

Quantifying Model Performance

With the fitting forms and parameters established, product isentrope prediction is a simple process where the only input parameters necessary are ρ_0 and D_0. We

13

list the steps for clarity:

1. Calculate S from measured or estimated fitted model inputs: ρ_0 and D_0.
2. Determine γ_s from Eq. 5 with parameters from Table 1 and S.
3. Find ν_s and $\Delta_s = \nu_s/\nu_0$ from Eq. 2 with γ_s and ν_0.
4. Calculate the evolution of $P(\Lambda)$ and $e(\Lambda)$ from Eqs. 8 and 9, respectively, with parameters from Eqs. 10, 11, and Table 1. The previously determined ν_s value can be used to yield the dimensional specific volume ν from Λ.

This approach is sufficient to fully specify the product isentrope. Figure 9 shows the performance of the fitted model against the JWL in P–ν, e–ν, and e–S space for Composition B explosive, a common formulation, with excellent agreement. Figure 10 shows the performance of the fitted model for several other major classes of explosive including liquid nitromethane, conventional HMX-based PBX 9501, insensitive TATB-based PBX 9502, and highly nonideal ANFO (ammonium nitrate and fuel oil). Excellent agreement is seen between the global fit and the JWLs for Comp B, PBX 9501, and ANFO. For insensitive PBX 9502, the global fit model prediction is low, lagging by about 20% in e–ν space, but the insensitive-specific fit is excellent.
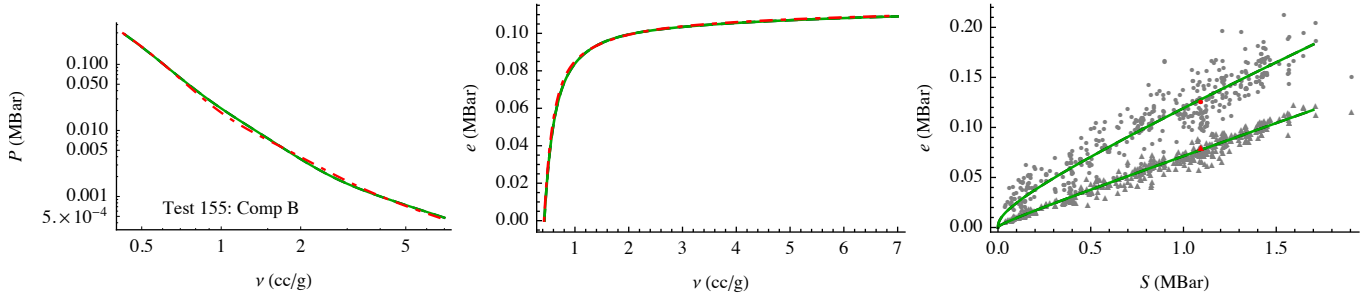
Figure 9: Isentrope predictions for Comp B from the global fitted (green) and JWL (red) models for pressure (left) and energy (center). The right plot shows energies at $\Lambda = 2$ (triangles) and $\Lambda = \infty$ (circles) with all JWL data in gray, the Comp B JWL in red, and the green overlaid curves representing the global fitted model prediction at each Λ value.

The resulting error distribution in energy δe from Eq. 6, equivalent to the integrated error in $\Delta_s P$, is unimodal (Fig. 11). The standard deviation σ of $\delta e(\Lambda)$ is 10.7% at $\Lambda = 1$ and asymptotically approaches 17% as $\Lambda \to \infty$ (Fig. 12). Evaluation of σ for the errors between the fitted model and JWLs quantifies the fitted model performance and indicates that the fitted model performance is consistent across the range of expansion values (Fig. 12).
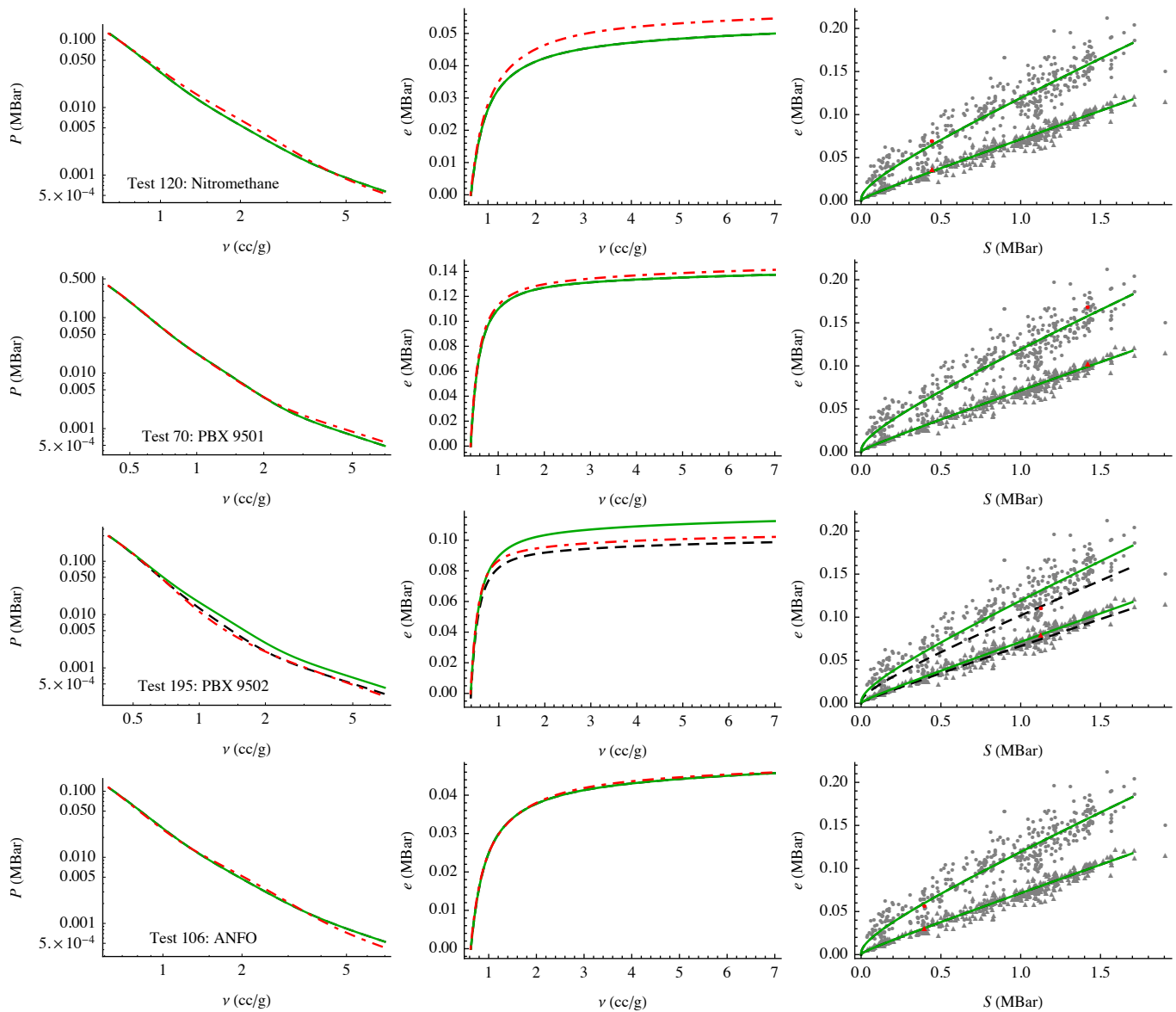
Figure 10: Each row shows model performance for the listed explosive with features as in Fig. 9. The dashed black curves for PBX 9502 are the fitted model prediction with the insensitive parameter estimates.

It is important to note that higher σ values can result not only from deficiencies in the fitted model, but also from inaccuracies in the derivation of each JWL. As discussed, JWL parameters are derived from hydrocode analysis of cylinder

15
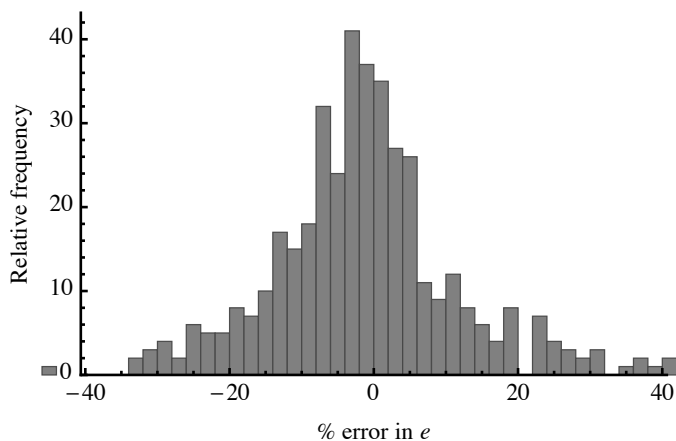
Figure 11: A histogram of the differences $\delta e(\Lambda = 7)$ between the fitted model and all JWLs with σ of 14.0%.

expansion test data with the total energy set by calorimetry or thermochemical equilibrium assumptions. The present dataset was collected over a 60-year period involving many different researchers, methods, diagnostics, and hydrocode models, which will inevitably result in data variations. As there is no practical way to evaluate the error associated with each JWL determination, we treat these data as given in the present study.

5. Conclusions

Several empirical correlations have been identified in prior detonation product equation-of-state (EOS) data that relate the reactant kinetic energy density to the mechanical energy for shock compression (Rayleigh energy), the heat of detonation, as well as the product energy and pressure during product expansion. These relationships were used to develop a universal detonation product equation of state that depends only on initial charge density and detonation velocity as inputs. The use of only two physically quantifiable EOS input parameters represents a dramatic simplification relative to existing models, which require measurement of up to seven formulation-specific parameters. This new result implies that the product energy density scales with the reactant kinetic energy. This scaling appears to apply to all known condensed-phase explosives tested to date. This relationship also indicates that explosive microstructural and chemical details only influence the product state though the density and detonation velocity. This result can thus

16
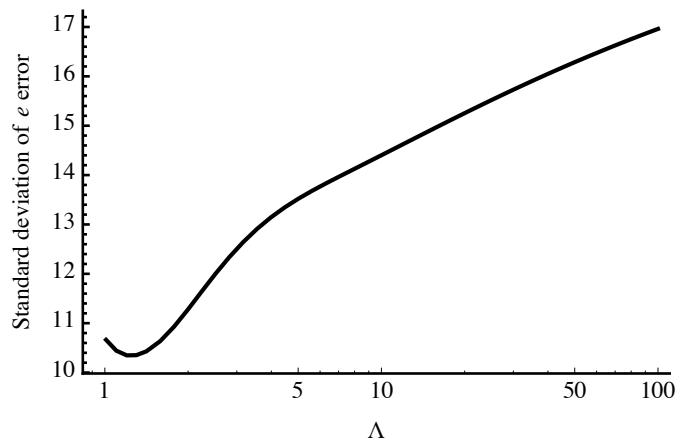
Figure 12: Standard deviation of the variation of the percent errors in energy with Λ.

be used to predict the heat of detonation from knowledge of the detonation velocity or, in turn, to predict the detonation velocity from thermochemical equilibrium product state assumptions. It may also be possible to combine it with curvature-based detonation theory [18, 19], which relates the local detonation shock curvature and velocity, to generate an equivalent relationship for shock curvature and energy release.

References

[1] C. Johansson, P. Persson, Density and pressure in the Chapman–Jouguet plane as functions of initial density of explosives, Nature 212 (5067) (1966) 1230–1231.

[2] M. J. Kamlet, S. Jacobs, Chemistry of detonations. I. A simple method for calculating detonation properties of C–H–N–O explosives, The Journal of Chemical Physics 48 (1) (1968) 23–35.

[3] P. Urtiew, B. Hayes, Parametric study of the dynamic JWL-EOS for detonation products, Combustion, Explosion, and Shock Waves 27 (4) (1991) 505–514.

[4] P. Urtiew, B. Hayes, Empirical estimate of detonation parameters in condensed explosives, Journal of Energetic Materials 9 (4) (1991) 297–317.

[5] M. Keshavarz, H. Pouretedal, An empirical method for predicting detonation pressure of CHNOFCl explosives, Thermochimica Acta 414 (2) (2004) 203–208.

[6] A. Koch, N. Arnold, M. Estermann, A simple relation between the detonation velocity of an explosive and its Gurney energy, Propellants, Explosives, Pyrotechnics 27 (6) (2002) 365–368.

[7] L. Fried, P. Souers, CHEETAH: A Next Generation Thermochemical Code, Tech. Rep. UCRL-117240, Lawrence Livermore National Laboratory, Livermore, 1994.

[8] F. Charlet, M.-L. Turkel, J.-F. Danel, L. Kazandjian, Evaluation of various theoretical equations of state used in calculation of detonation properties, Journal of Applied Physics 84 (8) (1998) 4227–4238.

[9] S. Jackson, The dependence of Ammonium-Nitrate Fuel-Oil (ANFO) detonation on confinement, Proceedings of the Combustion Institute 36 (2) (2017) 2791–2798.

[10] G. Taylor, Analysis of the explosion of a long cylindrical bomb detonated at one end, Mechanics of Fluids, Scientific Papers of GI Taylor 2 (1941) 277–286.

[11] E. Lee, H. Horning, J. Kury, Adiabatic expansion of high explosives detonation products, Tech. Rep. TID 4500-UCRL 50422, Lawrence Livermore National Laboratory, University of California, Livermore, CA, 1968.

[12] S. Jackson, An analytic method for two-dimensional wall motion and product isentrope from the detonation cylinder test, Proc. Combust. Inst. 35 (2) (2015) 1997–2004.

[13] W. Davis, 3: Shock Waves, Rarefaction Waves, Equations of State, in: W. W. J.A. Zukas (Ed.), Explosive Effects and Applications, chap. 3, Springer, 47–112, 1998.

[14] D. Ornellas, J. Carpenter, S. Gunn, Detonation Calorimeter and Results Obtained with Pentaerythritol Tetranitrate (PETN), The Review of Scientific Instruments 37 (7) (1966) 907–912.

[15] B. Wescott, D. Stewart, W. Davis, Equation of state and reaction rate for condensed-phase explosives, Journal of Applied Physics 98 (5) (2005) 053514.

[16] D. Ornellas, Calorimetric Determinations of the Heat and Products of Detonation for Explosives: October 1961 to April 1982, Tech. Rep. UCRL-52821, Lawrence Livermore National Laboratory, Livermore, CA, 1982.

[17] W. Fickett, W. Davis, Detonation: Theory and Experiment, Dover Publications, Inc., Mineola, NY, 1979.

[18] J. Bdzil, Steady-state two-dimensional detonation, Journal of Fluid Mechanics 108 (1981) 195–226.

[19] S. Jackson, M. Short, Scaling of detonation velocity in cylinder and slab geometries for ideal, insensitive and non-ideal explosives, Journal of Fluid Mechanics 773 (2015) 224–266.

[20] B. Dobratz, P. Crawford, LLNL Handbook of Explosives, Tech. Rep. UCRL-52997, Lawrence Livermore National Laboratory, 1985.

[21] R. Simpson, P. Urtiew, D. Ornellas, G. Moody, K. Scribner, D. Hoffman, CL-20 performance exceeds that of HMX and its sensitivity is moderate, Propellants, Explosives, Pyrotechnics 22 (5) (1997) 249–255.

[22] B. Dobratz, Properties of chemical explosives and explosive simulants, Tech. Rep. UCRL-5319, University of California, Livermore (USA). Lawrence Livermore Laboratory, 1972.

[23] R. Simpson, R. Garza, M. Foltz, D. Ornellas, P. Utriew, Characterization of TNAZ, Tech. Rep. UCRL-ID-119672, Lawrence Livermore National Lab., CA (United States), 1994.

[24] C. M. Tarver, P. A. Urtiew, W. C. Tao, Shock initiation of a heated ammonium perchlorate-based propellant, Combustion and Flame 105 (1) (1996) 123–131.

[25] H. Hansson, Determination of properties for emulsion explosives using cylinder expansion tests and numerical simulation, Tech. Rep. 2009:1, ISSN 1653-5006, Swedish Blasting Research Centre och Luleå tekniska universitet (Swebrec), 2009.

[26] W. Tao, C. Tarver, J. Kury, C. Lee, D. Ornellas, Understanding composite explosive energetics: 4. reactive flow modeling of aluminum reaction kinetics in PETN and TNT using normalized product equation of state, in: Tenth Symposium (International) on Detonation, 628–636, 1993.

[27] C. Tarver, L. Green, Using small scale tests to estimate the failure diameter of a propellant, in: Ninth Symposium (International) on Detonation, 701–710, 1989.

[28] F. Shen, H. Wang, J.-F. Yuan, Different Diameter Cylinder Tests and Numerical Simulation of RDX based Aluminized Explosive, Hanneng Cailiao Chinese Journal of Energetic Materials 21 (6) (2013) 777–780.

[29] L. Chen, The cylinder test and JWL equation of state detonation product of aluminized explosives, Huozhayao Xuebao Chinese Journal of Explosives and Propellants 24 (3) (2001) 3–15.

[30] E. Lee, M. Finger, W. Collins, JWL equation of state coefficients for high explosives, Tech. Rep. UCID-16189, Lawrence Livermore National Laboratory, 1973.

[31] M. Murphy, R. Simpson, R. Breithaupt, C. Tarver, Reactive flow measurements and calculations for ZRH_2-based composite explosives, in: Ninth Symposium (International) on Detonation, 525–534, 1989.

[32] R. Simpson, P. Urtiew, D. Ornellas, G. Moody, K. Scribner, D. Hoffman, CL-20 performance exceeds that of HMX and its sensitivity is moderate, Propellants, Explosives, Pyrotechnics 22 (5) (1997) 249–255.

[33] S. Karlsson, H. Östmark, C. Eldsäter, T. Carlsson, H. Bergman, S. Wallin, A. Pettersson, Detonation and sensitivity properties of FOX-7 and formulations containing FOX-7, in: Proc. 20th International Detonation Symposium, San Diego, CA, August, 286–291, 2002.

[34] W. A. Trzciński, S. Cudziło, Z. Chyłek, L. Szymańczyk, Detonation properties of 1, 1-diamino-2, 2-dinitroethene (DADNE), Journal of Hazardous Materials 157 (2) (2008) 605–612.

[35] W. A. Trzciński, L. Szymańczyk, Detonation properties of low-sensitivity NTO-based explosives, Journal of Energetic Materials 23 (3) (2005) 151–168.

[36] P. W. Merchant, S. J. White, A. M. Collyer, A WBL-consistent JWL equation of state for the HMX-based explosive EDC37 from cylinder tests, in: Proc. 12th International Detonation Symposium, San Diego, CA, August, 11–16, 2002.

[37] R. Winter, L. Markland, S. Prior, Modelling shock initiation of HMX-based explosive, in: AIP Conference Proceedings, vol. 505, AIP, 883–886, 2000.

[38] K. S. Vandersall, C. M. Tarver, F. Garcia, S. K. Chidester, On the low pressure shock initiation of octahydro-1,3,5,7-tetranitro-1,3,5,7-tetrazocine based plastic bonded explosives, Journal of Applied Physics 107 (9) (2010) 094906.

[39] H. Hornberg, F. Volk, The cylinder test in the context of physical detonation measurement methods, Propellants, Explosives, Pyrotechnics 14 (5) (1989) 199–211.

[40] P. Souers, J. Kury, Comparison of cylinder data and code calculations for homogeneous explosives, Propellants, Explosives, Pyrotechnics 18 (4) (1993) 175–183.

[41] B. W. White, C. M. Tarver, Ignition and growth modeling of detonation reaction zone experiments on single crystals of PETN and HMX, in: AIP Conference Proceedings, vol. 1793, AIP Publishing, 030001, 2017.

[42] K.-Y. Tan, Y. Han, G. Luo, M. Yin, Y.-M. Huang, X.-J. Lu, Power Ability and JWL Equation of State of a HMX-based PBX, Chinese Journal of Explosives and Propelants 36 (3) (2013) 42–45.

[43] P. A. Urtiew, K. S. Vandersall, C. M. Tarver, F. Garcia, J. W. Forbes, Shock initiation experiments and modeling of Composition B and C-4, in: Thirteenth International Detonation Symposium, 929–939, 2006.

[44] J. Forbes, C. Tarver, G. Urtiew, et al., The effects of confinement and temperature on the shock sensitivity of solid explosives, in: The Eleventh Symposium (International) on Detonation, 145–152, 1998.

[45] C. Tarver, Modeling detonation experiments on triaminotrinitrobenzene (TATB)-based explosives LX-17, PBX 9502, and ultrafine TATB, Journal of Energetic Materials 30 (3) (2012) 220–251.

[46] C. M. Tarver, W. C. Tao, C. G. Lee, Sideways plate push test for detonating solid explosives, Propellants, Explosives, Pyrotechnics 21 (5) (1996) 238–246.

[47] C. Tarver, J. Forbes, F. Garcia, P. Urtiew, Manganin gauge and reactive flow modeling study of the shock initiation of PBX 9501, in: AIP Conference Proceedings, vol. 620, AIP, 1043–1046, 2002.

[48] H. O. Wooten, V. H. Whitley, Analysis of historical and recent PBX 9404 cylinder tests using FLAG, Tech. Rep. LA-UR-16-24389, Los Alamos National Laboratory, 2016.

[49] H. O. Wooten, T. D. Aslam, V. H. Whitley, iVCJ: A tool for Interactive Visualization of high explosives CJ states, Tech. Rep. LA-UR-16-29341, Los Alamos National Laboratory, 2016.

[50] E. L. Lee, C. M. Tarver, Phenomenological model of shock initiation in heterogeneous explosives, The Physics of Fluids 23 (12) (1980) 2362–2372.

[51] T. Hussain, Y. Liu, F. Huang, Z. Duan, Ignition and growth modeling of shock initiation of different particle size formulations of PBXC03 explosive, Journal of Energetic Materials 34 (1) (2016) 38–48.

[52] C. Tarver, L. Erickson, N. Parker, Shock initiation, detonation wave propagation and metal acceleration measurements and calculations for RX-26-AF, Shock Compression of Condensed Matter (1983) 609.

[53] E. Lee, J. Walton, P. Kramer, Equation of state for the detonation products of hexanitrostilbene at various charge densities, Tech. Rep., California Univ., Livermore (USA). Lawrence Livermore Lab., 1976.

[54] C. M. Tarver, S. K. Chidester, Ignition and growth modeling of short pulse shock initiation experiments on fine particle Hexanitrostilbene (HNS), in: Journal of Physics: Conference Series, vol. 500, IOP Publishing, 052044, 2014.

[55] C. M. Tarver, P. A. Urtiew, T. D. Tran, Sensitivity of 2,6-Diamino-3,5-Dinitropyrazine-1-Oxide, Journal of Energetic Materials 23 (3) (2005) 183–203.

[56] S. Esen, P. Souers, P. Vitello, Prediction of the non-ideal detonation performance of commercial explosives using the DeNE and JWL++ codes, International Journal for Numerical Methods in Engineering 64 (14) (2005) 1889–1914.

[57] S. Jackson, The dependence of Ammonium-Nitrate Fuel-Oil (ANFO) detonation on confinement, Proceedings of the Combustion Institute 36 (2) (2017) 2791–2798.

[58] L. L. Davis, L. G. Hill, ANFO cylinder tests, in: AIP Conference Proceedings, vol. 620, AIP, 165–168, 2002.

[59] P. Souers, D. Larson, C. Carver, Performance calculations on the ANFO explosive RX-HD, in: Proceedings of the Symposium on the Non-Proliferation Experiment: Results and Implications for Test Ban Treaties, April 19-21, Rockville, MD, 4–9 to 4–37, 1994.

[60] K.-H. Kim, J. J. Yoh, A particle level-set based Eulerian method for multi-material detonation simulation of high explosive and metal confinements, Proceedings of the Combustion Institute 34 (2) (2013) 2025–2033.

[61] R. Garza, F. Helm, P. Souers, R. Simpson, Performance properties of the emulsion explosive QM-100, Tech. Rep. UCRL-ID-112431, Lawrence Livermore National Lab., CA (United States), 1992.

[62] C. Tarver, A. Lefrancois, R. Lee, K. Vandersall, Shock initiation of the PETN-based Explosive LX-16, in: Thirteenth International Detonation Symposium, 881–889, 2006.

[63] K. T. Lorenz, E. L. Lee, R. Chambers, A simple and rapid evaluation of explosive performance–The disc acceleration experiment, Propellants, Explosives, Pyrotechnics 40 (1) (2015) 95–108.

[64] J. Lu, F. Christo, D. Kennedy, Detonation modelling of corner-turning shocks in PBXN-111, Ph.D. thesis, DSTO, 2004.

[65] P. C. Souers, R. Garza, H. Hornig, L. Lauderbach, C. Owens, P. Vitello, Metal Angle Correction in the Cylinder Test, Propellants, Explosives, Pyrotechnics 36 (1) (2011) 9–15.

[66] P. Souers, L. Haselman Jr, Detonation equation of state at LLNL, 1993, Tech. Rep. UCRL-ID-119262, Lawrence Livermore National Lab., CA (United States), 1994.

[67] N. Coleburn, H. Jones, H. Sternberg, Initiation, Detonation Propagation, and Computational Studies for Submunitions Containing Amatex-20, Tech. Rep. NSWC/WOL/TR 75-94, Naval Surface Weapons Center, White Oak Lab, Silver Spring, MD, 1976.

[68] M. Murphy, E. Lee, A. Weston, A. Williams, Modeling shock initiation in Composition B, in: Tenth Symposium (International) on Detonation, 963–970, 1993.

[69] K. S. Vandersall, F. Garcia, C. M. Tarver, Shock initiation experiments with ignition and growth modeling on low density composition B, in: AIP Conference Proceedings, vol. 1793, AIP Publishing, 040015, 2017.

[70] P. Elek, V. Džingalašević, S. Jaramaz, D. Micković, Cylinder test: Analytical and numerical modeling, 4th International Scientific Conference on Defensive Technologies 1 (2) (2011) 2.

[71] J. P. Lu, D. L. Kennedy, Modeling of PBX-115 using kinetic CHEETAH and the DYNA codes, Tech. Rep. DSTO-TR-1496, Defense Science and Technology Organization Salisbury (Australia) Systems Sciences Lab, 2003.

[72] A. Mitchell, P. Pagoria, C. Coon, E. Jessop, J. Poco, C. Tarver, R. Breithaupt, G. Moody, Nitroureas 1. Synthesis, scale-up and characterization of K-6, Propellants, Explosives, Pyrotechnics 19 (5) (1994) 232–239.

[73] S. Cudzilo, W. A. Trzcinski, A study on detonation characteristics of pressed NTO, Journal of Energetic Materials 19 (1) (2001) 1–21.

[74] R. Simpson, P. Urtiew, C. Tarver, Shock initiation of 1,3,3-trinitroazetidine (TNAZ), in: AIP Conference Proceedings, vol. 370, AIP, 883–886, 1996.

[75] C. Tarver, M. E.M., Reactive Flow Modeling of the Interaction of TATB detonation waves with inert materials, in: Twelfth International Detonation Symposium, 641–649, 2002.

[76] A. N. Hodgson, C. A. Handley, DSD/WBL-consistent JWL equations of state for EDC35, in: AIP Conference Proceedings, vol. 1426, AIP, 247–250, 2012.

[77] C. M. Tarver, J. W. Kury, R. D. Breithaupt, Detonation waves in tri-aminotrinitrobenzene, Journal of Applied Physics 82 (8) (1997) 3771–3782.

[78] K. Vandersall, F. Garcia, C. Tarver, L. Fried, Shock Desensitization Experiments and Reactive Flow Modeling on Self-Sustaining LX-17 Detonation Waves, in: Thirteenth International Detonation Symposium, 333–340, 2014.

[79] K. Bahl, R. Breithaupt, C. Tarver, W. Von Holle, Fabry-Perot Velocimetry on Detonating LX-17 in Planar and Spherically Divergent Geometries, in: Ninth Symposium (International) on Detonation, 131–141, 1989.

[80] E. Topkaraoğlu, Design and development of a cylinder expansion test setup for determination of equation of state parameters of various explosives, Ph.D. thesis, Middle East Technical University, 2014.

[81] J. W. Kury, R. D. Breithaupt, C. M. Tarver, Detonation waves in trinitro-toluene, Shock Waves 9 (4) (1999) 227–237.

[82] P. Urtiew, C. Tarver, R. Simpson, Shock initiation of 2, 4-dinitroimidazole (2, 4-DNI), in: AIP Conference Proceedings, vol. 370, AIP, 887–890, 1996.

[83] M. A. Price, A. H. Ghee, Modeling for detonation and energy release from peroxides and non-ideal improvised explosives, Central European Journal of Energetic Materials 6 (3-4) (2009) 239–254.

Appendix A. Data Tables

Table A.2: Calorimetry data paired with detonation velocity data.

Test #	HE Name	ρ_0 (g/cc)	D_0 (cm/μs)	S (MBar)	Δh_d (MBar)	D_0 Ref.	Δh_d Ref.
1	CL-20	1.956	0.92	1.656	0.122	[20]	[21]
2	HMX	1.89	0.905	1.548	0.117	[20]	[16]
3	HMX	0.73	0.48	0.168	0.040	[20]	[16]
4	HMX	1.2	0.652	0.510	0.066	[20]	[16]
5	Octol 74-26	1.81	0.8346	1.261	0.103	[20]	[16]
6	PBX 9404	1.8	0.866	1.350	0.104	[20]	[22]
7	HNS	1.649	0.705	0.820	0.083	[20]	[16]
8	HNS	1.017	0.472	0.227	0.037	[20]	[16]
9	NM	1.13	0.628	0.446	0.056	[20]	[16]
10	NM	1.13	0.628	0.446	0.058	[20]	[16]
11	Pentolite	1.65	0.752	0.933	0.085	[20]	[22]
12	PETN	1.735	0.822	1.172	0.108	[20]	[16]
13	PETN	1.705	0.811	1.121	0.105	[20]	[16]
14	PETN	1.705	0.811	1.121	0.106	[20]	[16]
15	PETN	1.705	0.811	1.121	0.106	[20]	[16]
16	PETN	1.705	0.811	1.121	0.107	[20]	[16]
17	XTX-8003	1.55	0.7313	0.829	0.075	[20]	[16]
18	Comp B	1.74	0.809	1.139	0.096	[20]	[16]
19	RDX	1.76	0.867	1.323	0.107	[20]	[16]
20	RDX	1.78	0.865	1.332	0.112	[20]	[22]
21	BTF	1.86	0.849	1.341	0.110	[22]	[20]
22	HNB	1.918	0.934	1.673	0.133	[20]	[20]
23	TNAZ	1.83	0.873	1.395	0.112	[23]	[23]
24	FEFO	1.6	0.745	0.888	0.086	[20]	[16]
25	TATB	1.87	0.762	1.086	0.080	[20]	[16]
26	TNT	1.533	0.671	0.690	0.069	[20]	[16]
27	TNT	1.54	0.672	0.695	0.070	[20]	[22]
28	TNT	1.533	0.671	0.690	0.070	[20]	[16]
29	TNT	1.53	0.67	0.687	0.068	[20]	[16]
30	TNT	0.998	0.507	0.257	0.036	[20]	[16]

Table A.3: JWL parameters.

Test #	HE Name	ρ_0 (g/cc)	D_0 (cm/μs)	S (MBar)	A (Mbar)	B (Mbar)	C (Mbar)	R_1	R_2	ω	ν_s (cc/g)	P_s (Mbar)	Ref.
1	ANB-3066	1.800	0.756	1.029	23.350	0.551	0.009	6.75	2.28	0.242	0.435	0.224	24
2	E682-a with Al	1.129	0.564	0.358	2.535	0.065	0.010	4.99	1.97	0.499	0.664	0.090	25
3	E682-a with Al	1.169	0.571	0.381	2.589	0.071	0.010	4.93	1.96	0.512	0.640	0.096	25
4	PETN/Al (80/20)	1.893	0.788	1.176	8.126	0.654	0.030	5.55	2.23	0.420	0.384	0.320	26
5	PETN/Al (90/10)	1.800	0.800	1.152	5.022	0.269	0.038	4.50	2.00	0.500	0.399	0.325	26
6	PETN/Al (95/5)	1.775	0.810	1.165	5.942	0.441	0.041	4.90	2.30	0.520	0.409	0.320	26
7	Propellant B	1.848	0.780	1.125	7.737	0.116	0.016	4.80	1.20	0.240	0.404	0.285	27
8	RDX-Al	1.868	0.749	1.047	5.030	0.120	0.019	4.40	1.15	0.330	0.385	0.294	28
9	RDX-Al	1.823	0.865	1.363	7.520	0.120	0.013	4.40	1.30	0.330	0.406	0.353	29
10	RX-04-DS	1.865	0.852	1.354	9.073	0.104	0.015	4.70	1.00	0.400	0.402	0.340	30
11	TNT/Al (90/10)	1.670	0.680	0.772	17.650	0.535	0.024	7.40	2.40	0.450	0.451	0.190	26
12	TNT/Al (95/5)	1.635	0.680	0.756	19.740	1.466	0.030	8.80	3.40	0.570	0.454	0.195	26
13	RX-25-BF	2.149	0.751	1.211	53.240	0.514	0.021	8.00	1.75	0.600	0.358	0.280	31
14	RX-25-BH	2.300	0.601	0.831	20.620	0.287	-0.023	7.00	1.00	0.600	0.325	0.210	31
15	LX-19	1.942	0.921	1.647	16.380	1.862	0.026	6.50	2.70	0.550	0.380	0.430	32
16	PBXC-19	1.896	0.908	1.564	26.440	0.268	0.027	6.13	1.50	0.500	0.411	0.345	32
17	FOX-7	1.756	0.836	1.229	9.986	0.088	0.015	4.93	1.12	0.401	0.418	0.292	33
18	FOX-7	1.780	0.832	1.234	14.140	0.217	0.012	5.54	1.51	0.320	0.412	0.284	34
19	CH30	1.810	0.858	1.332	13.220	0.252	0.009	5.36	1.46	0.310	0.420	0.319	35
20	EDC-11	1.776	0.821	1.197	7.008	0.121	0.005	4.50	1.10	0.300	0.417	0.311	30
21	EDC-24	1.783	0.873	1.359	9.433	0.088	0.011	4.70	0.90	0.350	0.422	0.335	30
22	EDC37	1.841	0.882	1.432	6.642	0.228	0.019	4.25	1.83	0.250	0.396	0.338	36
23	EDC37	1.842	0.880	1.425	8.524	0.180	0.012	4.60	1.30	0.380	0.402	0.370	37
24	EDC37	1.841	0.878	1.421	16.690	0.597	0.021	5.90	2.10	0.450	0.413	0.340	38
25	HMX	1.891	0.911	1.569	7.783	0.071	0.006	4.20	1.00	0.200	0.387	0.420	20
26	HMX	1.891	0.911	1.569	7.783	0.168	0.011	4.27	1.34	0.400	0.387	0.420	39
27	HMX	1.891	0.911	1.569	7.783	0.071	0.006	4.20	1.00	0.300	0.387	0.420	39
28	HMX	1.894	0.910	1.568	8.581	0.075	0.008	4.31	0.80	0.300	0.392	0.405	40
29	HMX	1.188	0.668	0.530	2.182	0.050	0.020	4.38	1.10	0.550	0.596	0.155	40
30	HMX	1.905	0.915	1.594	14.030	0.999	0.016	5.90	2.10	0.570	0.385	0.424	41
31	HMX/Binder (90/10)	1.725	0.872	1.311	6.814	0.101	0.012	4.30	1.25	0.300	0.430	0.344	42
32	LX-04	1.865	0.847	1.338	7.337	0.041	0.015	4.30	0.94	0.350	0.400	0.340	39
33	LX-04	1.865	0.847	1.338	8.364	0.130	0.015	4.62	1.25	0.420	0.400	0.340	39
34	LX-04	1.868	0.847	1.339	13.320	0.740	0.015	5.90	2.10	0.450	0.399	0.342	43
35	LX-04	1.770	0.870	1.340	13.640	0.718	0.015	5.90	2.10	0.450	0.422	0.339	44
36	LX-04	1.865	0.847	1.338	8.364	0.130	0.015	4.62	1.25	0.420	0.400	0.340	20
37	LX-07	1.865	0.864	1.392	8.710	0.139	0.009	4.60	1.15	0.300	0.399	0.355	20
38	LX-07	1.865	0.864	1.392	6.727	0.076	0.012	4.16	1.09	0.350	0.394	0.370	39
39	LX-07	1.865	0.864	1.392	6.867	0.079	0.011	4.20	1.00	0.400	0.394	0.370	39
40	LX-07	1.850	0.870	1.399	8.710	0.139	0.010	4.60	1.15	0.300	0.402	0.358	38
41	LX-09	1.840	0.884	1.438	7.508	0.078	0.015	4.28	1.08	0.350	0.402	0.375	39
42	LX-09	1.840	0.884	1.438	8.481	0.171	0.013	4.58	1.25	0.400	0.402	0.375	39
43	LX-09	1.840	0.884	1.438	8.481	0.171	0.013	4.58	1.25	0.400	0.402	0.375	20
44	LX-10	1.864	0.882	1.450	7.595	0.057	0.015	4.25	1.00	0.350	0.398	0.375	39
45	LX-10	1.864	0.882	1.450	8.807	0.190	0.013	4.62	1.32	0.380	0.398	0.375	39
46	LX-10	1.865	0.882	1.451	8.807	0.184	0.013	4.62	1.32	0.380	0.398	0.375	20
47	LX-11	1.875	0.832	1.298	7.791	0.107	0.009	4.50	1.15	0.300	0.398	0.330	20
48	LX-14	1.835	0.880	1.421	7.215	0.050	0.015	4.20	0.97	0.350	0.403	0.370	39
49	LX-14	1.835	0.880	1.421	8.261	0.172	0.013	4.55	1.32	0.380	0.403	0.370	39
50	LX-14	1.770	0.862	1.314	7.616	0.146	0.016	4.55	1.32	0.380	0.418	0.342	45
51	LX-14	1.835	0.880	1.421	16.690	0.597	0.021	5.90	2.10	0.450	0.415	0.340	46
52	LX-14	1.835	0.883	1.431	7.560	0.227	0.010	4.44	1.50	0.300	0.400	0.381	46
53	LX-14	1.835	0.883	1.431	31.040	1.744	0.013	7.66	2.65	0.400	0.409	0.358	46
54	LX-14	1.835	0.880	1.421	8.261	0.172	0.013	4.55	1.32	0.380	0.403	0.370	20

Table A.3: JWL parameters (cont).

Test #	HE Name	ρ_0 (g/cc)	D_0 (cm/μs)	S (MBar)	A (Mbar)	B (Mbar)	C (Mbar)	R_1	R_2	ω	ν_s (cc/g)	P_s (Mbar)	Ref.
55	Octol 78-22	1.821	0.848	1.309	7.486	0.134	0.012	4.50	1.20	0.380	0.406	0.342	20
56	PBX 9011	1.777	0.850	1.284	6.347	0.080	0.007	4.20	1.00	0.300	0.414	0.340	20
57	PBX 9051	1.838	0.873	1.402	16.690	0.597	0.018	5.90	2.10	0.450	0.415	0.334	47
58	PBX 9404	1.845	0.877	1.419	9.290	0.275	0.012	4.85	1.45	0.280	0.401	0.370	48
59	PBX 9404	1.845	0.875	1.412	7.300	0.235	0.011	4.45	1.45	0.280	0.396	0.382	48
60	PBX 9404	1.843	0.885	1.445	8.500	0.205	0.016	4.60	1.49	0.280	0.402	0.374	48
61	PBX 9404	1.847	0.891	1.468	7.600	0.245	0.010	4.45	1.50	0.280	0.395	0.396	48
62	PBX 9404	1.847	0.891	1.467	7.600	0.250	0.012	4.46	1.50	0.280	0.396	0.395	48
63	PBX 9404	1.845	0.883	1.438	7.697	0.204	0.014	4.46	1.49	0.280	0.398	0.382	48
64	PBX 9404	1.845	0.883	1.438	7.697	0.204	0.014	4.46	1.49	0.280	0.398	0.381	48
65	PBX 9404	1.845	0.883	1.438	7.697	0.204	0.014	4.46	1.49	0.280	0.399	0.380	48
66	PBX 9404	1.843	0.878	1.421	7.624	0.224	0.015	4.50	1.50	0.280	0.398	0.380	49
67	PBX 9404	1.842	0.880	1.425	8.524	0.180	0.012	4.60	1.30	0.380	0.402	0.370	50
68	PBX 9404	1.840	0.880	1.425	8.524	0.180	0.012	4.60	1.30	0.380	0.402	0.370	20
69	PBX 9501	1.840	0.880	1.425	8.524	0.180	0.012	4.55	1.30	0.380	0.402	0.370	20
70	PBX 9501	1.834	0.880	1.420	7.781	0.209	0.015	4.50	1.50	0.280	0.401	0.375	49
71	PBX 9501	1.832	0.881	1.421	16.690	0.597	0.021	5.90	2.10	0.450	0.415	0.340	38
72	PBX-9011	1.770	0.850	1.279	6.048	0.050	0.012	4.10	1.00	0.350	0.415	0.340	39
73	PBX-9011	1.770	0.850	1.279	6.347	0.080	0.007	4.20	1.00	0.300	0.415	0.340	39
74	PBX-9404	1.840	0.880	1.425	7.469	0.069	0.014	4.27	1.06	0.350	0.402	0.370	39
75	PBX-9404	1.840	0.880	1.425	8.524	0.180	0.012	4.60	1.30	0.380	0.402	0.370	39
76	PBXC03	1.849	0.873	1.408	10.250	0.226	0.009	4.91	1.37	0.290	0.405	0.354	51
77	RX-05-DR	1.711	0.796	1.084	5.267	0.068	0.010	4.20	1.05	0.360	0.428	0.290	30
78	RX-06-AF	1.658	0.780	1.009	5.030	0.091	0.008	4.30	1.10	0.350	0.441	0.270	30
79	RX-08-AC	1.794	0.844	1.278	6.527	0.097	0.012	4.30	1.10	0.350	0.409	0.340	30
80	RX-08-BV	1.810	0.860	1.339	6.699	0.129	0.011	4.30	1.20	0.300	0.404	0.360	30
81	RX-08-DW	1.845	0.856	1.352	7.145	0.159	0.011	4.40	1.30	0.320	0.424	0.294	30
82	RX-26-AF	1.838	0.825	1.252	8.018	0.526	0.011	5.00	2.10	0.340	0.403	0.325	52
83	HNS	1.000	0.510	0.260	1.627	0.108	0.007	5.40	1.80	0.250	0.712	0.075	20
84	HNS	1.400	0.634	0.563	3.665	0.068	0.012	4.80	1.40	0.320	0.530	0.145	20
85	HNS	1.650	0.703	0.815	4.631	0.089	0.013	4.55	1.35	0.350	0.446	0.215	20
86	HNS	1.200	0.574	0.395	2.479	0.036	0.013	4.86	1.17	0.350	0.612	0.105	39
87	HNS	1.600	0.695	0.773	4.092	0.018	0.015	4.30	0.84	0.350	0.463	0.200	39
88	HNS	1.200	0.574	0.395	2.631	0.072	0.009	5.00	1.50	0.300	0.612	0.105	39
89	HNS	1.600	0.695	0.773	4.606	0.073	0.013	4.60	1.30	0.350	0.463	0.200	39
90	HNS	1.655	0.703	0.818	4.238	0.031	0.017	4.33	1.00	0.400	0.445	0.215	40
91	HNS	1.001	0.510	0.260	1.388	0.028	0.007	4.66	1.00	0.350	0.719	0.073	40
92	HNS	1.000	0.510	0.260	1.627	0.108	0.007	5.40	1.80	0.250	0.712	0.075	53
93	HNS	1.200	0.574	0.395	2.631	0.072	0.009	5.00	1.50	0.300	0.612	0.105	53
94	HNS	1.400	0.634	0.563	3.665	0.068	0.012	4.80	1.40	0.320	0.530	0.145	53
95	HNS	1.600	0.695	0.773	4.606	0.073	0.013	4.60	1.30	0.350	0.463	0.200	53
96	HNS	1.650	0.703	0.815	4.631	0.089	0.013	4.55	1.35	0.350	0.446	0.215	53
97	HNS	1.600	0.680	0.740	5.363	0.270	0.015	5.40	1.80	0.450	0.456	0.200	54
98	LLM-105	1.880	0.806	1.221	7.196	0.138	0.010	4.50	1.50	0.310	0.397	0.310	55
99	AN emulsion	1.150	0.592	0.403	2.844	0.028	0.008	4.80	1.20	0.310	0.654	0.100	56
100	ANFO	0.873	0.409	0.146	3.380	0.130	0.009	7.74	3.09	0.590	0.816	0.042	57
101	ANFO	0.865	0.428	0.158	0.854	0.182	0.010	5.91	3.39	0.390	0.763	0.054	57
102	ANFO	0.782	0.508	0.202	0.876	0.008	0.007	4.31	0.89	0.170	0.930	0.055	39
103	ANFO	0.782	0.508	0.202	0.752	-0.008	0.012	4.31	1.25	0.440	0.930	0.055	39
104	ANFO	0.930	0.416	0.161	0.495	0.019	0.005	3.91	1.12	0.333	0.731	0.052	58
105	ANFO	1.320	0.700	0.647	4.825	0.141	0.002	5.08	2.00	0.550	0.570	0.160	59
106	ANFO	1.160	0.585	0.397	2.988	0.041	0.007	4.95	1.15	0.350	0.621	0.111	60
107	ANFO	0.800	0.451	0.163	1.463	0.011	0.008	5.50	1.00	0.290	0.927	0.042	56
108	Aquanal	1.430	0.370	0.196	0.925	0.006	0.008	4.37	0.77	0.350	0.503	0.055	39

Table A.3: JWL parameters (cont).

Test #	HE Name	ρ_0 (g/cc)	D_0 (cm/μs)	S (MBar)	A (Mbar)	B (Mbar)	C (Mbar)	R_1	R_2	ω	ν_s (cc/g)	P_s (Mbar)	Ref.
109	Aquanal	1.430	0.370	0.196	0.913	0.004	0.007	4.40	1.00	0.160	0.503	0.055	39
110	E682-a	1.129	0.564	0.358	2.535	0.065	0.010	4.99	1.97	0.499	0.664	0.090	25
111	E682-a	1.169	0.571	0.381	2.589	0.071	0.010	4.93	1.96	0.512	0.640	0.096	25
112	E682-b	1.180	0.587	0.406	2.857	0.067	0.010	4.93	1.96	0.520	0.637	0.101	25
113	Pourvex	1.360	0.610	0.506	2.724	0.013	0.008	4.30	0.86	0.250	0.546	0.130	39
114	Pourvex	1.360	0.610	0.506	3.221	0.078	0.003	4.70	1.40	0.160	0.546	0.130	39
115	QM-100	1.260	0.626	0.493	4.870	0.025	0.005	5.00	1.00	0.300	0.589	0.127	60
116	QM-100	1.261	0.626	0.494	3.637	0.097	0.006	5.00	1.55	0.220	0.592	0.125	61
117	Unigel	1.294	0.548	0.388	1.218	0.019	0.006	3.60	0.86	0.350	0.534	0.120	39
118	Unigel	1.294	0.548	0.388	1.907	0.076	0.006	4.40	1.40	0.230	0.534	0.120	39
119	LX-01	1.230	0.684	0.575	3.110	0.048	0.010	4.50	1.00	0.350	0.594	0.155	20
120	Nitromethane	1.128	0.628	0.445	2.092	0.057	0.008	4.40	1.20	0.300	0.637	0.125	20
121	Nitromethane	1.130	0.628	0.446	2.978	0.060	0.011	5.03	1.10	0.490	0.647	0.120	40
122	Nitromethane	1.128	0.629	0.446	2.035	0.036	0.010	4.29	1.08	0.350	0.638	0.125	39
123	Nitromethane	1.128	0.629	0.446	2.093	0.057	0.008	4.40	1.20	0.300	0.638	0.125	39
124	RX-01-AE	1.210	0.611	0.452	2.111	0.048	0.008	4.30	1.30	0.340	0.598	0.125	30
125	Detasheet	1.480	0.720	0.767	3.738	0.036	0.001	4.20	1.10	0.300	0.495	0.205	59
126	EL-506A	1.480	0.720	0.767	3.738	0.036	0.011	4.20	1.10	0.300	0.495	0.205	20
127	EL-506C	1.480	0.700	0.725	3.490	0.045	0.009	4.10	1.20	0.300	0.494	0.195	20
128	LX-16	1.700	0.796	1.078	5.168	0.245	0.011	4.50	1.50	0.290	0.422	0.305	62
129	LX-17	1.734	0.815	1.153	9.582	0.908	0.002	5.95	2.65	0.555	0.427	0.300	63
130	Pentolite 50/50	1.700	0.753	0.964	5.409	0.094	0.013	4.50	1.10	0.350	0.432	0.255	20
131	Pentolite 50/50	1.700	0.753	0.964	5.409	0.094	0.001	4.50	1.10	0.350	0.433	0.255	59
132	Pentolite 50/50	1.650	0.736	0.894	5.318	0.089	0.010	4.60	1.05	0.330	0.447	0.235	64
133	PETN	0.880	0.517	0.235	3.486	0.113	0.009	7.00	2.00	0.240	0.836	0.062	20
134	PETN	1.260	0.654	0.539	5.731	0.211	0.001	6.00	1.80	0.280	0.587	0.140	20
135	PETN	1.500	0.745	0.833	6.253	0.233	0.012	5.25	1.60	0.280	0.491	0.220	20
136	PETN	1.770	0.830	1.219	6.170	0.169	0.007	4.40	1.20	0.250	0.410	0.335	20
137	PETN	1.770	0.830	1.219	6.704	0.104	0.016	4.44	1.19	0.310	0.417	0.320	39
138	PETN	1.770	0.830	1.219	7.965	0.192	0.007	4.80	1.20	0.250	0.417	0.320	39
139	PETN	1.763	0.827	1.207	10.320	0.906	0.037	6.00	2.60	0.570	0.419	0.315	40
140	PETN	1.503	0.748	0.841	3.511	0.057	0.012	4.08	0.90	0.350	0.475	0.240	40
141	PETN	1.263	0.659	0.548	2.282	0.051	0.014	4.24	1.05	0.350	0.561	0.160	40
142	PETN	1.765	0.829	1.212	7.295	0.178	0.013	4.68	1.32	0.310	0.417	0.319	65
143	PETN	1.750	0.835	1.220	6.170	0.169	0.007	4.40	1.20	0.250	0.414	0.335	50
144	PETN	1.778	0.832	1.231	10.510	0.934	0.037	6.00	2.60	0.570	0.416	0.321	41
145	PETN	1.762	0.827	1.206	10.290	0.907	0.002	6.00	2.60	0.570	0.419	0.315	63
146	PETN	1.763	0.827	1.207	10.320	0.906	0.037	6.00	2.60	0.570	0.419	0.315	26
147	PETN	1.000	0.555	0.308	2.372	0.106	0.010	5.60	1.80	0.240	0.724	0.085	66
148	PETN	1.600	0.725	0.842	6.253	0.233	0.013	5.25	1.60	0.280	0.459	0.223	66
149	Explosive D	1.420	0.650	0.600	3.007	0.039	0.010	4.30	1.20	0.350	0.516	0.160	20
150	Amatex-20	1.603	0.703	0.792	4.952	0.081	0.012	4.60	1.00	0.350	0.463	0.220	67
151	C-4	1.601	0.819	1.075	6.098	0.130	0.010	4.50	1.40	0.250	0.462	0.280	55
152	C30	1.717	0.785	1.058	9.862	0.135	0.012	5.21	1.30	0.320	0.443	0.253	35
153	CB	1.674	0.783	1.026	7.053	0.119	0.013	4.80	1.31	0.330	0.447	0.259	35
154	Comp A-3	1.650	0.830	1.137	6.113	0.107	0.011	4.40	1.20	0.320	0.446	0.300	20
155	Comp B	1.717	0.798	1.093	4.964	0.039	0.013	4.06	0.95	0.350	0.425	0.295	39
156	Comp B	1.717	0.798	1.093	5.242	0.076	0.011	4.20	1.10	0.340	0.425	0.295	20
157	Comp B	1.694	0.788	1.051	5.798	0.114	0.019	4.50	1.50	0.280	0.435	0.276	49
158	Comp B	1.717	0.809	1.125	5.242	0.077	0.016	4.20	1.10	0.500	0.424	0.306	55
159	Comp B	1.630	0.770	0.966	5.575	0.078	0.013	4.50	1.20	0.340	0.455	0.250	68
160	Comp B	1.200	0.631	0.477	2.447	0.396	0.016	6.20	2.20	0.500	0.568	0.152	69
161	Comp B	1.500	0.719	0.775	5.047	0.665	0.014	6.20	2.20	0.500	0.466	0.233	69
162	Comp C-4	1.601	0.819	1.075	6.098	0.130	0.010	4.50	1.40	0.250	0.462	0.280	20

Table A.3: JWL parameters (cont).

Test #	HE Name	ρ_0 (g/cc)	D_0 (cm/μs)	S (MBar)	A (Mbar)	B (Mbar)	C (Mbar)	R_1	R_2	ω	ν_s (cc/g)	P_s (Mbar)	Ref.
163	Comp. B (60:40)	1.666	0.780	1.014	4.553	0.045	0.013	4.08	0.98	0.350	0.437	0.276	39
164	Comp. B (64:36)	1.717	0.798	1.093	5.242	0.077	0.011	4.20	1.10	0.340	0.425	0.295	39
165	Cyclotol	1.754	0.825	1.194	5.600	0.051	0.014	4.12	1.00	0.350	0.417	0.320	39
166	Cyclotol	1.754	0.825	1.194	6.034	0.099	0.011	4.70	1.10	0.350	0.417	0.320	39
167	Cyclotol 77/23	1.754	0.825	1.194	6.034	0.099	0.011	4.30	1.10	0.350	0.417	0.320	20
168	FH5	1.600	0.793	1.006	5.734	0.010	0.008	4.28	0.32	0.218	0.470	0.250	70
169	H-6	1.760	0.747	0.982	7.581	0.085	0.011	4.90	1.10	0.200	0.430	0.240	20
170	PBX 9010	1.787	0.839	1.258	5.814	0.068	0.002	4.10	1.00	0.350	0.409	0.340	20
171	PBX 9407	1.600	0.791	1.001	5.732	0.146	0.012	4.60	1.40	0.320	0.459	0.265	20
172	PE-4	1.590	0.813	1.051	7.741	0.087	0.013	4.84	1.07	0.284	0.474	0.259	71
173	BTF	1.859	0.848	1.337	8.407	0.150	0.014	4.60	1.20	0.300	0.393	0.360	20
174	BTF	1.852	0.849	1.335	9.456	0.227	0.030	5.03	1.60	0.500	0.402	0.340	40
175	C50	1.738	0.773	1.039	9.515	0.126	0.011	5.16	1.33	0.300	0.439	0.247	35
176	CH50	1.825	0.845	1.303	13.860	0.253	0.009	5.46	1.46	0.310	0.418	0.310	35
177	HNB	1.965	0.934	1.714	10.480	0.080	0.014	4.47	0.85	0.280	0.381	0.430	40
178	K-6	1.857	0.904	1.517	9.459	1.335	0.017	5.40	2.60	0.350	0.396	0.400	72
179	NTO	1.770	0.794	1.116	10.250	0.085	0.007	5.03	1.20	0.250	0.436	0.254	73
180	TNAZ	1.830	0.803	1.181	10.330	0.906	0.037	6.00	2.60	0.570	0.405	0.306	74
181	FEFO	1.590	0.750	0.894	3.824	0.066	0.014	4.10	1.20	0.380	0.453	0.250	20
182	FEFO	1.607	0.745	0.892	4.053	0.042	0.014	4.15	0.84	0.400	0.451	0.245	40
183	FM-1	1.509	0.657	0.651	2.673	0.078	0.017	4.28	1.23	0.480	0.469	0.190	40
184	EDC35	1.900	0.771	1.128	13.620	0.720	0.009	6.20	2.20	0.500	0.396	0.280	75
185	EDC35	1.910	0.779	1.158	8.209	0.098	0.002	4.68	1.13	0.300	0.397	0.281	76
186	LX-17	1.905	0.758	1.094	13.450	0.673	0.010	6.20	2.20	0.500	0.395	0.270	77
187	LX-17	1.905	0.763	1.109	14.810	0.638	0.009	6.20	2.20	0.500	0.400	0.265	78
188	LX-17	1.905	0.768	1.124	14.810	0.638	0.011	6.20	2.20	0.500	0.399	0.270	45
189	LX-17	1.905	0.763	1.109	5.314	0.027	0.013	4.10	1.10	0.460	0.388	0.290	66
190	LX-17	1.905	0.759	1.098	43.430	1.946	0.023	8.50	3.28	0.600	0.405	0.250	66
191	LX-17	1.905	0.760	1.099	16.690	0.486	0.015	6.20	2.20	0.500	0.406	0.250	46
192	LX-17	1.905	0.760	1.099	4.603	0.095	0.013	4.00	1.70	0.480	0.382	0.300	46
193	LX-17	1.905	0.760	1.099	5.314	0.027	0.012	4.10	1.10	0.460	0.386	0.290	46
194	LX-17-0	1.900	0.760	1.097	4.460	0.013	0.013	3.85	1.03	0.460	0.383	0.300	20
195	PBX 9502	1.895	0.771	1.126	4.603	0.095	0.013	4.00	1.70	0.480	0.386	0.302	20
196	PBX 9502	1.895	0.772	1.128	13.620	0.720	0.009	6.20	2.20	0.500	0.397	0.280	45
197	TATB	1.830	0.758	1.051	6.868	0.078	0.009	4.60	1.20	0.300	0.411	0.260	40
198	TATB	1.900	0.760	1.096	6.547	0.071	0.008	4.45	1.20	0.350	0.394	0.275	50
199	Ultrafine TATB	1.800	0.746	1.001	12.050	0.603	0.013	6.20	2.20	0.500	0.417	0.249	45
200	Ultrafine TATB	1.800	0.748	1.007	4.978	0.054	0.011	4.20	1.20	0.400	0.409	0.265	79
201	X-0219	1.920	0.753	1.089	8.268	0.085	0.008	4.80	1.20	0.350	0.396	0.260	30
202	Tetryl	1.730	0.791	1.082	5.868	0.011	0.008	4.40	1.20	0.280	0.426	0.285	20
203	TNT	1.630	0.693	0.783	3.712	0.032	0.010	4.15	0.95	0.300	0.449	0.210	20
204	TNT	1.612	0.692	0.772	4.213	0.095	0.013	4.50	1.50	0.280	0.457	0.204	49
205	TNT	1.630	0.693	0.783	3.620	0.025	0.009	4.03	0.89	0.200	0.449	0.210	39
206	TNT	1.630	0.693	0.783	3.712	0.032	0.010	4.15	0.95	0.300	0.449	0.210	39
207	TNT	1.590	0.663	0.699	4.531	0.156	0.006	5.15	1.00	0.344	0.446	0.203	80
208	TNT	1.632	0.707	0.816	5.244	0.049	0.006	4.58	0.85	0.230	0.459	0.205	40
209	TNT	1.610	0.697	0.783	3.712	0.032	0.010	4.15	0.95	0.300	0.454	0.210	50
210	TNT	1.624	0.685	0.762	6.731	0.220	0.011	5.40	1.80	0.300	0.462	0.190	81
211	TNT	1.645	0.693	0.790	33.950	0.822	0.020	8.30	2.80	0.600	0.469	0.180	66
212	TNT-AN (50:50)	1.633	0.633	0.653	3.310	0.065	0.007	4.33	1.26	0.350	0.448	0.175	39
213	TNT-Nigu (50:50)	1.665	0.730	0.887	4.699	0.083	0.008	4.37	1.25	0.350	0.442	0.234	39
214	TNT-Nigu (65:35)	1.658	0.705	0.824	3.899	0.083	0.009	4.26	1.23	0.350	0.438	0.226	39
215	TNT-Nigu-Al (42:31:27)	1.849	0.695	0.894	6.116	0.047	0.006	4.59	1.18	0.350	0.411	0.214	39
216	TNT-Nigu-Al (50:35:15)	1.745	0.707	0.873	4.980	0.064	0.007	4.42	1.21	0.350	0.427	0.223	39

Table A.3: JWL parameters (cont).

Test #	HE Name	ρ_0 (g/cc)	D_0 (cm/μs)	S (MBar)	A (Mbar)	B (Mbar)	C (Mbar)	R_1	R_2	ω	ν_s (cc/g)	P_s (Mbar)	Ref.
217	1,2-DP	1.260	0.597	0.449	1.677	0.036	0.014	4.12	1.00	0.330	0.555	0.135	40
218	2,4-DNI	1.670	0.825	1.137	6.113	0.107	0.011	4.40	1.20	0.320	0.441	0.300	82
219	DIPAM	1.550	0.670	0.696	4.254	0.080	0.012	4.70	1.30	0.390	0.478	0.180	20
220	HMTD	0.800	0.434	0.151	0.732	0.013	0.007	4.70	1.02	0.310	0.886	0.044	83
221	PF	1.833	0.729	0.974	4.184	0.051	0.018	4.11	0.95	0.650	0.394	0.270	40
222	TATP	0.600	0.318	0.061	0.246	0.006	0.005	4.93	0.94	0.150	1.118	0.020	83